

Enhanced O_2^+ Loss at Mars due to an Ambipolar Electric Field from Electron Heating

R. E. Ergun^{1,2}, L. A. Andersson², C. M. Fowler^{1,2}, A. K. Woodson², T. D. Weber², G. T.
Delory³, D. J. Andrews⁴, A. I. Eriksson⁴, T. McEnulty², M. W. Morooka², A. I. F.
Stewart², P.R. Mahaffy⁵, and B. M. Jakosky²

Corresponding author: Robert E. Ergun, Laboratory of Atmospheric and Space Sciences,
University of Colorado, Boulder, Colorado, USA 80303. ree@lasp.colorado.edu.

¹Department of Astrophysical and Planetary Sciences, University of Colorado, Boulder,
Colorado, USA.

²Laboratory of Atmospheric and Space Sciences, University of Colorado, Boulder,
Colorado, USA

³Space Sciences Laboratory, University of California, Berkeley, California, USA

⁴Swedish Institute of Space Physics (Uppsala), Uppsala, Sweden

⁵Planetary Environments Laboratory, Code 699, NASA Goddard Space Flight Center,
Greenbelt, MD.

Key Points:

Enhanced O_2^+ loss at Mars

Ambipolar electric field at Mars

Abstract

Recent results from the MAVEN Langmuir Probe and Waves (LPW) instrument suggest higher than predicted electron temperatures (T_e) in Mars' dayside ionosphere above ~ 180 km in altitude. Correspondingly, measurements from Neutral Gas and Ion Mass Spectrometer (NGIMS) indicate significant abundances of O_2^+ up to ~ 500 km in altitude, suggesting that O_2^+ may be a principal ion loss mechanism of oxygen. In this article, we investigate the effects of the higher T_e (which results from electron heating) and ion heating on ion outflow and loss. Numerical solutions show that plasma processes including ion heating and higher T_e may greatly increase O_2^+ loss at Mars. In particular, enhanced T_e in Mars' ionosphere just above the exobase creates a substantial ambipolar electric field with a potential ($e\Phi$) of several $k_B T_e$, which draws ions out of the region allowing for enhanced escape. With active solar wind, electron and ion heating, direct O_2^+ loss could match or exceed loss via dissociative recombination of O_2^+ . These results suggest that direct loss of O_2^+ may have played a significant role in the loss of oxygen at Mars over time.

1. Introduction

Spacecraft and lander observations have provided strong evidence that Mars once had surface water and an atmosphere that is now lost, entreating one of the most intriguing questions in planetary science: how did Mars loose its atmosphere and water? Isotopic ratios give evidence of substantial loss to space [*Pepin*, 1994] whereas present-day in-situ observations indicate on-going loss at rates that are substantially lower than that needed for the inferred atmosphere and water loss.

The combination of Mars' weak gravitational binding and photochemical and plasma processes may be central to explaining Mars' atmospheric loss. The present-day photochemical loss is dominated by dissociative recombination of O_2^+ [e. g. *McElroy*, 1972; *Rohrbaugh et al.*, 1979; *Barth*, 1985; *Nagy and Cravens*, 1988; *Fox and Hac*, 2009], which creates a hot O corona about Mars. This process is primarily limited by the solar UV intensity, which, by some estimates, could have been as much as five to ten times higher four billion years ago [*Bressan et al.*, 1993; *Ayres*, 1997; *Sackmann and Boothroyd*, 2003; *Lundin et al.*, 2007]. Even with enhanced UV, however, this process would be responsible for loss of less than 1 m of surface water from Mars over 4 Gyr [*Lillis et al.*, 2015].

In situ observations of ion fluxes indicate that present-day ion loss is a fraction of that from dissociative recombination [e. g., *Lundin et al.*, 2004; *Barabash et al.*, 2007].

Fluxes of O^+ , O_2^+ and CO_2^+ have been measured in space and appear to be highly variable and often sporadic. Escape rates are difficult to quantify due to returning fluxes [e. g. *Brain et al.*, 2015]. Stronger fluxes have been associated with stronger solar wind

activity (e. g. velocity, energy flux, magnetic field strength), albeit the association is not well understood and is a topic of current studies [e. g. *Lundin et al.*, 2004].

The role of O_2^+ in photochemical loss is well documented [*Hanson et al.*, 1977; more references can be found in recent reviews, e.g. *Nagy et al.* 2004; *Witasse et al.*, 2008; *Withers*, 2009]. O_2^+ dissociative recombination appears to be the major, present-day loss mechanism. Recent spacecraft observations [*Kar et al.*, 1996; *Bougher et al.*, 2015] indicate that direct loss of O_2^+ is less but significant. *Fox* [1997] suggested that O_2^+ might be the major escaping ion if escape is at maximum rates. Interestingly, [*Kar et al.*, 1996] indicated that O_2^+ escape could be supported at observed rates [*Lundin et al.*, 1989; 1990] if given a 1 km/s acceleration at the top side of Mars' ionosphere. We intend to demonstrate that an ambipolar electric field can provide such acceleration.

Recent measurements of the electron temperature (T_e) altitude profile [*Ergun et al.*, 2015] reveal higher values of T_e (~ 0.3 eV) in the dayside ionosphere above 200 km than that predicted (~ 1 eV) by modeling [e. g. *Withers et al.*, 2014], supporting the early observations of Viking at altitudes above ~ 200 km [*Hanson and Mantas*, 1988]. Several numerical models [*Chen et al.*, 1978; *Choi et al.*, 1998; *Matta et al.*, 2014; *Withers et al.*, 2014; *Cui et al.*, 2015] have demonstrated that solar heating is insufficient to reproduce the elevated T_e as observed by *Hanson and Mantas* [1988]. The elevated dayside T_e , now confirmed, is not fully understood; an electron heating mechanism has not been identified.

In this article, we focus on a major consequence of the elevated electron temperatures; the ambipolar electric field that retains the electrons also accelerates ions out of the ionosphere. We examine present day and past O_2^+ escape with an ambipolar

electric field using recent MAVEN observations to guide Combined Photochemistry and Ion Tracing (CAPIT) simulations [Andersson *et al.*, 2010].

A critical region for photochemical loss is the region surrounding the exobase. An exobase is defined for a particular species. Since we are examining several species, we use the term “exobase” to describe the boundary between collision-dominated photochemical processes (low altitude) and the higher-altitude ionosphere where plasma processes appear to play a dominant role. Under this definition, the exobase at Mars is between ~180 km and ~220 km in altitude, depending on species and the conditions of the neutral atmosphere.

Photochemical reactions are most intense well below the exobase due to the high density of the neutral atmosphere. In addition, ionization from UV fluxes is strongest below the exobase. Mars’ atmosphere is optically thin above ~160 km. However, photochemical interactions at low altitudes primarily influence the local ion constituency. For example, at ~160 km in altitude, the mean free path of O_2^+ is less than 1 km so the products of photochemical reactions remain localized and do not directly result in escape. On the other hand, ions or energized neutrals that are created from photochemical reactions above the exobase are free to travel long distances. However, the rapidly decreasing density of the neutral atmosphere greatly reduces the ion production rates and other photochemical reaction rates above the exobase. As a result, the region surrounding the exobase (within a few scale heights) is critical to ion loss.

The CAPIT code focuses on this region. We use the CAPIT code to demonstrate that the ambipolar electric field created through elevated electron temperatures (electron heating) may be responsible for enhanced, present-day O_2^+ loss. Furthermore, under

extreme solar conditions, O_2^+ loss can exceed loss of oxygen via dissociative recombination of O_2^+ by more than an order of magnitude. Therefore, it is possible that direct O_2^+ loss may have played an important role in the loss of oxygen at Mars.

There are a plethora of processes that can influence ion escape. For example, the magnetic field [Acuna *et al.*, 1998; 1999] near the exobase can play a critical role [e.g., Hanson and Mantas, 1988; Choy *et al.*, 1998; Krymskii *et al.*, 2003; Duru *et al.*, 2006; Lillis *et al.*, 2011; Matta *et al.*, 2015]. A horizontal magnetic field binds ions and electrons to the altitude at which they were created. At Mars, the draped magnetic field is expected to have a small flare angle that directs ion flow from the dayside to the night side with a slow rise in altitude. This long escape path causes ions to dwell in the ionosphere for long periods increasing the possibility of recombination or subsequent photochemical processes, thus reducing escape.

The composition of the neutral atmosphere can influence oxygen escape. For example, the ratio of O to CO_2 densities influences O_2^+ production. The state of the solar wind, its wave activity, the electric field penetration into the ionosphere, and the ionizing fluxes of electrons and ions also can influence escape. In this article, we concentrate on photochemical processes and plasma processes in the region surrounding the exobase to understand the controlling factors in this region.

2. MAVEN Observations

MAVEN observations from the Langmuir Probe and Waves (LPW) instrument [Andersson *et al.*, 2015; Ergun *et al.*, 2015] and the Neutral Gas and Ion Mass Spectrometer (NGIMS) [Mahaffy *et al.*, 2015b] are displayed with CAPIT simulations in both panels of Figure 1. The CAPIT simulations are discussed below. The MAVEN data

have been previously published [Ergun *et al.*, 2015; Lillis *et al.*, 2015; Brougher *et al.*, 2015], so our description is brief. Observations are from April 17, 2015 to April 22, 2015 during a “deep dip” campaign when MAVEN probed to altitudes just below 130 km with low solar zenith angle, less than 15° at the lowest altitudes [see Ergun *et al.*, 2015 for orbital coverage]. The solar UV intensity was moderate and the solar wind activity was moderate.

Figure 1 (left) displays the altitude profile of the electron density (black circles with error bars) derived from the LPW observations and averaged over the inbound part of twenty-two orbits during a deep dip campaign [Ergun *et al.*, 2015]. By comparison with electron density (n_e) determined by wave sounding [Andersson *et al.*, 2015], the LPW n_e , at the lowest altitudes, is estimated to be within -25% to + 10% as indicated by the error bars. At low altitudes, below ~ 180 km, n_e measurements are fairly repeatable from orbit to orbit. Within an orbit, there was small variation. Above ~ 300 km in altitude, the n_e variations are very strong, occasionally over an order of magnitude from orbit to orbit and within an orbit. These data reflect the expectation that photochemical processes dominate n_e below ~ 180 km, which leads to low variability, whereas plasma processes appear to be active above that altitude leading to higher variability.

The green circles represent the O_2^+ density as measured by the NGIMS instrument [Mahaffy *et al.*, 2015b]. The blue circles represent the O^+ density and the red circles represent the CO_2^+ density. The NGIMS observations are the average density over the same inbound legs of the twenty-two orbits during the deep-dip campaign. NGIMS has excellent relative accuracy but requires a baseline for absolute accuracy. NGIMS densities best correspond to the LPW densities if adjusted higher by a factor of ~ 1.5 for

all species. The adjustment is not applied in Figure 1. The good qualitative agreement of the altitude profiles between LPW and NGIMS (total density) gives confidence that the observations reflect the average structure of Mars' ionosphere. The NGIMS observations also show the same variation pattern as the LPW observations: relatively low variation below ~ 180 km and very strong variation above ~ 300 km. The observations show enhanced O_2^+ densities at high altitude, that is the high-altitude densities are well above standard scale-height expectations, supporting earlier observations from the Phobos 2 mission [e. g. *Kar et al.*, 1996] and photochemical models [e. g. *Fox*, 1997].

The measured electron temperature (T_e) profile from MAVEN LPW displayed in Figure 1 right shows enhanced temperatures (~ 0.3 eV) from that predicted by photochemical models at ~ 0.1 eV [*Chen et al.*, 1978; *Choi et al.*, 1998; *Matta et al.*, 2014; *Withers et al.*, 2014], indicating an electron energy source. One possibility is that the electron energy may come from plasma wave heating. Alternatively, the enhanced T_e may be due to transport of hot, shocked solar wind electrons to the ionosphere. The high-altitude (above the exobase) T_e observations are in good agreement with T_e measured by the Viking 1 lander [*Hanson and Mantas*, 1988].

The high values of T_e in the exobase region have several important consequences. An ambipolar electric field with a potential ($e\Phi$) on the order of several times $k_B T_e$ is required to retain the electrons. This same electric field will energize ions in the exobase region and draw them into the upper ionosphere. For example, an ambipolar potential of ~ 0.6 V will allow an O_2^+ ion at ~ 200 km to overcome gravitational potential and travel up to ~ 1000 km in altitude. Once drawn out the exobase region, photochemical loss and recombination are dramatically lowered due to the lower densities and higher T_e . Ion

heating through plasma waves can act to add energy to these ions so the likelihood of escape can dramatically increase.

3. CAPIT Model

Several models have included higher T_e and the ambipolar potential either via a fluid approach [e.g. *Fox*, 1997 and citations within], MHD models [e. g. *Ma et al.* 2002; 2014, and citations within], or with hybrid models [e.g. *Brecht and Ledvina*, 2014 and citations within]. The hybrid approaches have coarse altitude resolution (> 10 km) restricting the accuracy in the exobase region. The CAPIT code is specifically designed to focus on the exobase and accurately trace ions.

The 2D CAPIT model is described by *Andersson et al.*, [2010]. We use a 1D version of CAPIT, which produces comparable results but allows for faster convergence and self-consistent treatment of low-frequency Poynting flux that heats ions. In this section, we briefly describe the CAPIT code and focus on the differences between the 1D CAPIT code and the previously published 2D CAPIT code [*Andersson et al.*, 2010].

The basic idea behind the CAPIT model is to examine the critical layer of the dayside ionosphere near the exobase. The CAPIT code simulates photochemical reactions on a grid while tracing ions in space. The neutral densities are prescribed and remain constant; they are not altered by photochemical reactions. The altitude profiles for CO_2 , O , N_2 , O_2 , NO , CO in this article have a density with a constant scale height derived from those in *Mahaffy et al.*, [2015a] and *Lillis et al.*, [2015], which are based on NGIMS observations during the same deep dip period that we examine.

Figure 2 shows the basic domain of the 1D CAPIT and 2D CAPIT codes. The 2D CAPIT code includes an extended region along the draped magnetic field (blue region in

Figure 2). The 1D CAPIT code emulates this draped magnetic field line starting at low solar zenith angle from low altitude (160 km in this article) to the top of the ionosphere (500 km in this article) where solar wind phenomena begin to dominate. CAPIT 1D uses a constant 10° (from horizontal) flare angle for the draped magnetic field. It allows for motion along the draped field line but does not allow for variation of densities or other parameters in the horizontal direction. Ion motion and the ambipolar electric field are restricted to be along the magnetic field. Ion motion is controlled by the electric field, magnetic field, plasma wave heating, gravity, and collisions.

The CAPIT code includes twenty-eight photochemical reactions relevant to the region above the primary ionosphere density peak (M2 peak, which is at ~ 130 km in altitude), detailed in Table 1. This set of interactions is expanded from that used by *Andersson et al.*, [2010] to include NO^+ and CO^+ . CAPIT does not include UV absorption, so it is primarily valid above ~ 160 km in altitude, where UV absorption is small. The mean free path of ions at ~ 160 km is less than 1 km, so it is adequate to simulate the upper part of the collisional ionosphere beginning at 160 km.

Both versions of the CAPIT code, 1D and 2D, have photoionization that operates in a grid. The grid point in the 1D code spans 1 km in altitude, which is 5.75 km along a field line (consistent with 10° flare angle). Every second, ions are created via random number based on the neutral densities, photoionization rates, and solar UV flux in each grid. The positions of ions within a grid are randomized and the velocities (parallel and perpendicular to the magnetic field) are also randomized to mimic a distribution at the same temperature as the neutral species that was ionized (300 °K for simulations in this article). Once an ion is created, its motion is determined by the electric field, the

223 magnetic field, gravity, wave heating, and collisions. Ions also undergo a set of
 224 photochemical interactions at the rates describe in Table 1, again at a one second
 225 cadence. The hot O products from dissociative recombination of O_2^+ are assigned an
 226 escape probability as a function of altitude to tabulate total loss via that process. The
 227 neutral density of O, however, is not changed.

Table 1: Photochemical Reactions used in 1D CAPIT

Reaction (Ionization)	Rate (s^{-1}) Moderate Sun	Reference
$N_2 + \gamma \rightarrow N_2^+ + e^-$	2.80×10^{-7}	<i>Huebner et al.</i> , 1992
$CO_2 + \gamma \rightarrow CO_2^+ + e^-$	5.30×10^{-7}	<i>Huebner et al.</i> , 1992
$O + \gamma \rightarrow O^+ + e^-$	2.00×10^{-7}	<i>Huebner et al.</i> , 1992
$O_2 + \gamma \rightarrow O_2^+ + e^-$	4.40×10^{-7}	<i>Huebner et al.</i> , 1992
$NO + \gamma \rightarrow NO^+ + e^-$	10.1×10^{-7}	<i>Huebner et al.</i> , 1992
$CO + \gamma \rightarrow CO^+ + e^-$	3.44×10^{-7}	<i>Huebner et al.</i> , 1992
Reaction (Electron)	Rate (cm^3/s)	Reference
$N_2^+ + e^- \rightarrow N + N$	$2.2 \times 10^{-7} (300/T_e)^{0.39}$	<i>Matta</i> , 2013
$CO_2^+ + e^- \rightarrow CO + O$	$4.2 \times 10^{-7} (300/T_e)^{0.75}$	<i>Matta</i> , 2013
$O^+ + e^- \rightarrow O$ (not included)	$3.26 \times 10^{-12} (300/T_e)^{0.7}$	<i>Matta</i> , 2013
$O_2^+ + e^- \rightarrow 2O$ (see note)	$2.4 \times 10^{-7} (300/T_e)^{0.7}$	<i>Matta</i> , 2013
$NO^+ + e^- \rightarrow NO$	$4.0 \times 10^{-7} (300/T_e)^{0.5}$	<i>Schunk and Nagy</i> , 2009
$CO^+ + e^- \rightarrow NO$	$2.75 \times 10^{-7} (300/T_e)^{0.55}$	<i>Schunk and Nagy</i> , 2009
Reaction	Rate at 300 °K (cm^3/s)	Reference
$N_2^+ + O \rightarrow O^+ + N_2$	9.8×10^{-12}	<i>Matta</i> , 2013
$N_2^+ + O \rightarrow NO^+ + N$	1.3×10^{-10}	<i>Matta</i> , 2013
$N_2^+ + NO \rightarrow NO^+ + N_2$	4.1×10^{-10}	<i>Schunk and Nagy</i> , 2009
$N_2^+ + O_2 \rightarrow O_2^+ + N_2$	5.0×10^{-11}	<i>Schunk and Nagy</i> , 2009
$N_2^+ + CO_2 \rightarrow O_2^+ + N_2$	8.0×10^{-10}	<i>Matta</i> , 2013
$CO^+ + O \rightarrow O^+ + CO$	1.4×10^{-10}	<i>Schunk and Nagy</i> , 2009
$CO^+ + CO_2 \rightarrow CO_2^+ + CO$	1.1×10^{-9}	<i>Schunk and Nagy</i> , 2009
$CO_2^+ + O \rightarrow O^+ + CO_2$	9.6×10^{-11}	<i>Matta</i> , 2013
$CO_2^+ + O \rightarrow O_2^+ + CO$	1.6×10^{-10}	<i>Matta</i> , 2013
$CO_2^+ + NO \rightarrow NO^+ + CO_2$	1.23×10^{-10}	<i>Schunk and Nagy</i> , 2009
$CO_2^+ + O_2 \rightarrow O_2^+ + CO_2$	5.0×10^{-11}	<i>Barth</i> , 1985
$O^+ + N_2 \rightarrow NO^+ + N$	1.2×10^{-12}	<i>Matta</i> , 2013
$O^+ + O_2 \rightarrow O_2^+ + O$	2.1×10^{-11}	<i>Schunk and Nagy</i> , 2009
$O^+ + NO \rightarrow NO^+ + O$	8.0×10^{-13}	<i>Schunk and Nagy</i> , 2009
$O^+ + CO_2 \rightarrow O_2^+ + CO$	1.1×10^{-9}	<i>Matta</i> , 2013
$O_2^+ + NO \rightarrow NO^+ + O_2$	4.6×10^{-10}	<i>Schunk and Nagy</i> , 2009

228

Ion motion is traced along a field line that is 10° from parallel to the surface. CAPIT 1D assumes a magnetic mirror ratio of 1.33 between 160 km and 500 km, corresponding to a reduction in strength of a factor of 0.75 in magnetic field. The mirror force is applied at each time step using the perpendicular velocity of the ion, altering the parallel and perpendicular velocity. The full gyration of the ion is not traced in the 1D code. The Collisions are treated as described in *Andersson et al.*, [2010]. Briefly, at each time step and for each ion, a random number is called and weighted with the neutral densities to determine if an ion is to undergo a collision. If a collision is called for, a neutral particle is created with a random velocity (speed and direction) consistent with the neutral temperature (300 °K). The impact parameter and azimuthal angle of the collision are also generated randomly. The ion-neutral collision acts to conserve momentum and energy and the ion is assigned a new velocity and direction in accordance to the collision. The neutral particle is then discarded, as there is no change in neutral densities and temperatures.

Wave heating is self-consistently implemented via a low-frequency Poynting flux introduced at the upper boundary [*Ergun et al.*, 2008; *Andersson et al.*, 2010]. The wave heating increases the perpendicular ion velocity; it does not directly affect the parallel velocity. The Poynting flux is depleted as it heats ions, conserving energy. This energy balance has an interesting effect as noted by *Andersson et al.* [2010]. The Poynting flux heats ions, which, through the mirror force, accelerates ions to higher altitudes. The enhanced ion densities at higher altitudes, in turn, absorb the Poynting flux before it reaches lower altitudes. This effect limits the how much Poynting flux can enhance outflow.

The electron temperature profile is prescribed in the 1D CAPIT code (Figure 1, right).

The analytic formula is taken from *Ergun et al.*, [2015]:

$$T_e = \frac{T_{eH} + T_{eL}}{2} + \frac{T_{eH} - T_{eL}}{2} \tanh\left(\frac{z - Z_o}{H_o}\right) \quad (1)$$

T_{eL} , the asymptotic value of T_e at the lowest altitudes, is set to 0.044 eV (510 °K). T_{eH} is the high-altitude asymptotic value of T_e , which is set to 0.271 eV (3140 °K). Z_o is set to 241 km. It represents the altitude of the most rapid change in T_e . Finally H_o , the scale height of the rapid change is set to 60 km. The fit is plotted in Figure 1 (right).

The ambipolar electric field (potential) is derived from the T_e and n_e profiles. The electron force equation parallel to the magnetic field and under equilibrium is [e.g. *Schunk and Nagy*, 2009; *Hartle and Grebowsky*, 1995]:

$$eE = -\partial P_e / \partial s \quad (2)$$

where $P_e = n_e k_B T_e$ is the electron pressure, e is the fundamental charge, s is coordinate in direction of the magnetic field, and k_B is the Boltzmann constant. In the 1 D CAPIT code, E is calculated from the derivative of a smoothed n_e and the assigned T_e profile. The electron density is derived from the ion density assuming a quasi-neutral plasma. The electric field is assumed to be along the magnetic field.

Outflow rates of the ions are estimated from transport at the high-altitude boundary of the simulation domain (500 km). Ions that pass through the boundary with sufficient kinetic energy to overcome gravitational binding are considered to have escaped; the flux

is designated as F_{min} . While it is possible that a fraction of these ions may return to the night-side ionosphere, we do not attempt to correct for such return flows, which may lead to an overestimate of the minimum escape. On the other hand, the majority of ions passing through the high-altitude boundary often do not have sufficient kinetic energy for escape. If the kinetic energy is such that the ion will return before reaching the terminator (~700 km in altitude; see Figure 1), its velocity is reversed and it reenters the simulation domain.

The remaining ions that pass through the high-altitude boundary, those with insufficient kinetic energy to overcome gravitational binding, may escape with additional heating or acceleration by the solar wind electric field. The escape probability of these ions leads to the largest uncertainty in our results. We assign the maximum outflow rate (F_{max}) as all ions passing through the high-altitude boundary with sufficient energy to reach the terminator (700 km in altitude, see Figure 2). We generate an “estimated” escape flux by assigning an escape probability (P) based on the kinetic energy (KE) of the outgoing ion and its gravitational binding energy ($W_{Gravity}$):

$$P = \frac{KE}{W_{Gravity}}, KE < W_{Gravity}; P = 1, KE \geq W_{Gravity} \quad (3)$$

F_{Est} , the estimated escape flux, is compiled by summing over the escape probabilities of all escaping ions. F_{Est} is plotted the nominal outflow rate. The escape probabilities are set so that estimated outflow rates from 1D CAPIT are similar to those predicted by 2D CAPIT and other models [e.g. Fox, 1997 and citations within]. The escape rates from 1D CAPIT are also within an order of magnitude of those estimated through measurements

[e. g. *Lundin et al.*, 2004; *Barabash et al.*, 2007; *Brain et al.*, 2015], we emphasize that, as with most modeling efforts, there is a significant quantitative uncertainty in determining escaped fluxes. The major conclusions of this article are based on the qualitative properties of the outflow.

4. Results

Figure 1 (left) displays results from CAPIT code as solid lines. The electron density is black, O_2^+ is green, O^+ is blue and CO_2^+ is red. The neutral O density was increased (by ~ 1.4) from that reported by Mahaffy et al. [2015a] and the low-frequency Poynting flux (ion heating) was adjusted to $3.16 \times 10^{-8} \text{ W/m}^2$ to obtain agreement between CAPIT and observations. Considering that the observations are averaged over 28 orbits, we find that the CAPIT results are in excellent qualitative agreement with the observed altitude profiles with quantitative differences, for the most part, less than a factor of 2. The primary differences are at high altitudes ($>200 \text{ km}$); CAPIT predicts slightly higher than observed densities of both O^+ and O_2^+ , but has excellent quantitative agreement with the LPW density. The NGIMS densities (O_2^+ , O^+ , and CO_2^+), however, were not adjusted to match the LPW electron density. Some difference is therefore expected.

The differences between the CAPIT results and NGIMS observations below $\sim 200 \text{ km}$ are from several factors. Since CAPIT does not have UV absorption, it predicts higher CO_2 ionization. The O^+ density profile at low altitudes is sensitive to the density profile of O, which is modeled from a single scale height whereas observations show a more complex structure. The O density profile also influences the O_2^+ density profile.

One of the most significant features of the 1D CAPIT model is its ability to examine the impact of the electron temperature profile on ion outflow. The ambipolar electric

field, which retains the electrons, will accelerate ions along a magnetic field to higher altitudes. Figure 3 (left) displays the outflow rates as a function of high-altitude electron temperature (T_{eH} in Equation 1) with weak low-frequency Poynting flux of 3.16×10^{-10} W/m². The colors represent species: purple is the estimated O outflow from dissociative recombination of O_2^+ , blue is O^+ outflow, green is O_2^+ outflow, and red is CO_2^+ outflow. The dashed lines show the maximum (F_{max}) and minimum (F_{min}) outflow rates as described in section 3.

There are several salient features in Figure 3 left. One can see a dramatic increase in the estimated O_2^+ outflow rates with increasing T_{eH} . F_{max} of O_2^+ increases to that of O^+ , nearly three orders of magnitude with the increase in T_{eH} . F_{min} , however, does increase but remains low indicating that most O_2^+ ions leaving the simulation domain do not have escape energy. Additional energy is needed for escape. It is clear that the ambipolar electric field rapidly draws O_2^+ from below the exobase (~ 200 km) to higher altitudes into a collisionless environment reducing recombination loss and dramatically increasing the possible direct ion outflow. CO_2^+ is also drawn out, but at significantly lower fluxes. Estimated and maximum O^+ outflow is increased, but not as dramatically as O_2^+ . O^+ is created at higher altitudes with peak densities above 250 km (Figure 1, left), which is already well above the exobase.

The right panel of Figure 3 displays outflow as a function of T_{eH} with nominal low-frequency Poynting flux (3.16×10^{-8} W/m²). Ion heating dramatically raises F_{max} at low values of T_{eH} . The results suggest that either ion heating or higher electron temperatures can increase possible outflow.

Figure 4 displays why both T_e and Poynting flux both must be considered when studying outflow. The left panel of Figure 4 displays estimated outflow as a function of low-frequency Poynting flux (ion heating rate) under a low T_{eH} (0.044 eV), and therefore a low ambipolar electric field. These results agree with those in *Andersson et al.*, [2010], who, using a 0.1 eV constant T_e , showed increasing O^+ and O_2^+ outflow with ion heating. In particular F_{max} of O_2^+ increases dramatically, allowing for possible larger escape. Figure 4 (right) displays a less intense increase in outflow when T_{eH} is set at the recently measured value (0.271 eV). The primary difference between the two plots comes from the stronger ambipolar electric field in the right plot, whereas the left plot, similar to that in *Andersson et al.* [2010], has a weak ambipolar electric field.

The estimated O outflow from dissociative recombination (purple squares) decreases with increasing T_{eH} and decreases with increasing Poynting flux. The decrease in dissociative recombination is due in part to the increase in T_{eH} but primarily from transport of O_2^+ out of the region near the exobase. Interestingly, the decrease in dissociative recombination appreciably offsets the increased outflow of oxygen atoms from ion outflow. In other words, the increase in O_2^+ outflow comes partly at the expense of dissociative recombination of O_2^+ .

5. Discussion and Past Outflow

The primary result from the simulations, constrained by MAVEN observations, is the strong sensitivity of O_2^+ outflow, in particular F_{max} , to the ambipolar electric field. The Poynting fluxes of low frequency plasma waves also increase outflow of all species as reported earlier [*Andersson et al.*, 2010]. These results demonstrate at least two

mechanisms in which ion heating or electron heating, presumably linked to increased solar wind activity, can enhance ion outflow.

The increased T_{eH} requires an energy source for electrons [e.g. *Schunk and Nagy*, 2009]. Modeling efforts [e.g. *Matta et al.*, 2014] predict that T_e is close to the neutral temperature (~ 0.026 eV) below ~ 125 km in altitude but rises quickly with altitude to ~ 0.1 eV. For $T_{eH} \sim 0.3$ eV, a heat source is required [*Chen et al.*, 1978; *Choi et al.*, 1998; *Matta et al.*, 2014; *Withers et al.*, 2014; *Cui et al.*, 2015]. Furthermore, the ambipolar electric field is energizing ions, so a continuous energy source into the electrons is required. One possibility is plasma wave heating in the topside ionosphere [e. g. *Ergun et al.*, 2006; *Schunk and Nagy*, 2009; *Andersson et al.*, 2010]. Another possibility is that hot, shocked solar wind electrons are transported into the topside ionosphere.

The early sun, roughly 4 Gyr ago, is estimated to have $\sim 70\%$ less luminosity but significantly higher output in ionizing radiation (in particular, UV) and significantly more energetic solar wind [*Bressan et al.*, 1993; *Ayres*, 1997; *Sackmann and Boothroyd*, 2003]. Fluxes of ionizing radiation are expected to be roughly five times the present day rate while the solar wind speed could be up to an order of magnitude higher. Solar wind forcing could enhance atmospheric escape in a variety of ways including penetration of the solar wind electric field, sputtering, and enhanced ion outflow [e. g. *Lundin et al.*, 2007].

Focusing on the critical region near the exobase, it is clear that a combination of increased photochemical production of ions and increased escape efficiency could greatly enhance escape. Figure 5 shows outflow rates as a function of enhanced solar activity using the present-day neutral atmosphere. In this figure, the solar UV flux (F_{UV}) is plotted

linearly. However, the solar wind energy flux is expected to increase more than linearly [Lundin *et al.*, 2007]. We increase the low-frequency Poynting flux as F_{UV}^2 assuming a linear increase in solar wind velocity and that the wave energy is proportional the solar wind energy flux. It is entirely possible that the solar wind density and magnetic field strength also increase, further increasing the solar wind energy flux. An increase in wave energy would increase the electron temperature as well. However, radiative cooling and other losses would limit the increase in T_e , so T_{eH} is increased as $F_{UV}^{1.5}$ whereas T_{eL} is increased linearly. The increases in T_e are not justified further and would be very difficult to rigorously defend. We present the estimated outflow rates with the given values of solar UV, Poynting flux, T_{eH} , and T_{eL} , which is one possible scenario that we investigate.

The color scheme in Figure 5 is identical to that in Figures 3 and 4. The horizontal axis shows the solar UV flux linearly, the Poynting flux, T_{eH} , and T_{eL} . The left panel has a magnetic field at 10° from horizontal; the right panel has a vertical magnetic field. At high solar UV fluxes and high solar wind forcing, the outflow of ions exceeds that of dissociative recombination by roughly an order of magnitude. F_{min} and F_{max} are nearly identical at high UV (high T_e) indicating that most O^+ , O_2^+ , and CO_2^+ ions that leave the simulation domain have escape energy. If T_{eH} exceeds ~ 1 eV, the ambipolar electric field can accelerate O_2^+ atoms to escape velocity.

With a 10° from horizontal magnetic field, the net outflow rate reaches $\sim 10^{13}$ oxygen Atoms/m²s ($\sim 3.3 \times 10^{26}$ Atom/s globally). This outflow rate can remove roughly 2 m of water in ~ 1 Gyr. The outflow rate is roughly four to five times higher if the magnetic

field is vertical. These results suggest that it is possible that ion outflow could have caused significant water or atmospheric loss at Mars.

There are many caveats to the simulations of the past outflow rates. The composition of the neutral atmosphere was certainly dissimilar to the present-day composition. The magnetic field structure has also dramatically changed. The solar UV flux and solar forcing parameters, while reasonable estimates with current knowledge, may have been substantially different. As such, our primary conclusions must be limited to the present-day exobase and the role of the ambipolar electric field.

6. Conclusions

CAPIT simulations focused on the exobase region and constrained by MAVEN observations, show that the ambipolar electric field from heated electrons can substantially increase ion outflow (O^+ , O_2^+ , and CO_2^+) in the present day. The maximum outflow rates increase dramatically, but additional energy is needed for escape. Our primary conclusion is that the combination of ion heating (low-frequency Poynting flux) and acceleration by the ambipolar electric field draws O^+ , O_2^+ and CO_2^+ from the exobase and can dramatically enhance ion outflow, in particular, outflow of O_2^+ .

We demonstrated a dramatic increase of ion outflow with electron heating and ion heating processes under stronger solar UV and solar wind forcing. Direct ion outflow exceeded that of dissociative recombination of O_2^+ . It is possible, then, that ion outflow could have been a significant factor in the loss of Mars' water and atmosphere.

Acknowledgments

The MAVEN project is supported by NASA through the Mars Exploration Program. Work at IRF was supported by grants from the Swedish National Space Board (DNR 162/14) and Vetenskapsdet (DNR 621-2014-5526). Data are from MAVEN LPW and NGIMS have been submitted to the NASA Planetary Data System. We thank Andy Nagy for his valuable help and insights.

References

- Acuna, M. H., et al. (1998), Magnetic field and plasma observations at Mars: Initial results of the Mars Global Surveyor mission, *Science*, 279, 1676–1680, doi:10.1126/science.279.5357.1676.
- Acuna, M. H., et al. (1999), Global distribution of crustal magnetization discovered by the Mars Global Surveyor MAG/ER experiment, *Science*, 284, 790–793, doi:10.1126/science.284.5415.790.
- Andersson, L., R. E. Ergun, and A. I. F. Stewart (2010), The combined atmospheric photochemistry and ion tracing code: Reproducing the Viking Lander results and initial outflow results, *Icarus*, 206, 120–129, doi:10.1016/j.icarus.2009.07.009.

449 Andersson, L., R. E. Ergun, G. Delory, A. I. Eriksson, J. Westfall, H. Reed, J. F. Mccauley,
 450 D. J. Summers, and D. Meyers (2015), The Langmuir Probe and Waves Experiment for
 451 MAVEN, *Space Science Reviews*.
 452 Ayres, T. (1997), Evolution of the solar ionizing flux, *J. Geophys. Res.*, 102, 1641–1651,
 453 doi:10.1029/96JE03306.
 454 Barabash, S., A. Fedorov, R. Lundin, and J. A. Sauvaud (2007), Martian atmospheric erosion
 455 rates, *Science*, 315, 501–503, doi:10.1126/science.1134358.
 456 Barth, C. A., 1985, The photochemistry of the atmosphere of Mars, In: Levine, J. S. (Ed.),
 457 The photochemistry of atmospheres: Earth, the other planets, and comets, *Academic*
 458 *Press. Inc.*, Orlando, pp 337-392.
 459 Brain, D. A., et al. (2015), The spatial distribution of planetary ion fluxes near Mars observed
 460 by MAVEN, *Geophys. Res. Lett.*, 42, doi:10.1002/2015GL065293.
 461 Bressan, A., F. Fagotto, G. Bertelli, C. Chiosi, (1993) Evolutionary sequences of stellar
 462 models with new radiative opacities. II - $Z = 0.02$, *Astron. Astrophys. Suppl. Ser.* 100,
 463 647–664.
 464 Brecht, S. H., and S. A. Ledvina (2014), The role of the Martian crustal magnetic fields in
 465 controlling ionospheric loss, *Geophys. Res. Lett.*, 41, 5340–5346,
 466 doi:10.1002/2014GL060841.
 467 Bougher, S., et al. (2015a), Early MAVEN deep dip campaign reveals thermosphere and
 468 ionosphere variability, *Science*, 350(6261), 0459, doi:10.1126/science.aad0459.
 469 Chaufray, J.-Y., F. Gonzalez-Galindo, F. Forget, M. Lopez-Valverde, F. Leblanc, R. Modolo,
 470 S. Hess, M. Yagi, P.-L. Blelly, and O. Witasse (2014), Three-dimensional Martian

471 ionosphere model: II. Effect of transport processes due to pressure gradients, *J. Geophys.*
 472 *Res. Planets*, 119, 1614–1636, doi:10.1002/2013JE004551.
 473 Chen, R. H., T. E. Cravens, and A. F. Nagy (1978), The Martian ionosphere in light of the
 474 Viking observations, *J. Geophys. Res.*, 83, 3871–3876, doi:10.1029/JA083iA08p03871.
 475 Choi, Y. W., J. Kim, K. W. Min, A. F. Nagy, and K. I. Oyama (1998), Effect of the magnetic
 476 field on the energetics of Mars ionosphere, *Geophys. Res. Lett.*, 25, 2753–2756,
 477 doi:10.1029/98GL51839.
 478 Cui, J., M. Galand, S. J. Zhang, E. Vigren, and H. Zou (2015), The electron thermal structure
 479 in the dayside Martian ionosphere implied by the MGS radio occultation data. *J.*
 480 *Geophys. Res. Planets*, 120, 278–286. doi: 10.1002/2014JE004726.
 481 Duru, F., D. A. Gurnett, T. F. Averkamp, D. L. Kirchner, R. L. Huff, A. M. Persoon, J. J.
 482 Plaut, and G. Picardi (2006), Magnetically controlled structures in the ionosphere of
 483 Mars, *J. Geophys. Res.*, 111, A12204, doi:10.1029/2006JA011975.
 484 Ergun, R. E., L. Andersson, W. K. Peterson, D. Brain, G. T. Delory, D. L. Mitchell, R. P.
 485 Lin, and A. W. Yau (2006), Role of plasma waves in Mars' atmospheric loss, *Geophys.*
 486 *Res. Lett.*, 33, L14103, doi:10.1029/2006GL025785.
 487 Ergun, R. E., M. W. Morooka, L. A. Andersson, C. M. Fowler, G. T. Delory, D. J. Andrews, A.
 488 I. Eriksson, T. McEnulty, and B. M. Jakosky (2015), Dayside electron temperature and
 489 density profiles at Mars: First results from the MAVEN Langmuir probe and waves
 490 instrument, *Geophys. Res. Lett.*, 42, doi:10.1002/2015GL065280.
 491 Fox, J. L. (1997), Upper limits to the outflow of ions at Mars: Implications for atmospheric
 492 evolution, *Geophys. Res. Lett.*, 24, 2901–2904, doi:10.1029/97GL52842.

493 Fox, J. L., and A. Hac (2009), Photochemical escape of oxygen from Mars: A comparison of
 494 the exobase approximation to a Monte Carlo method, *Icarus*, 204, 527–544,
 495 doi:10.1016/j.icarus.2009.07.05.
 496 Haider, S. A., S. P. Seth, E. Kallio, and K. I. Oyama (2002), Solar EUV and electron-proton-
 497 hydrogen atom-produced ionosphere on Mars: Comparative studies of particle fluxes and
 498 ion production rates due to different processes, *Icarus*, 159, 18 – 30.
 499 Hanson, W. B., S. Sanatani, and D. R. Zuccaro (1977), The Martian ionosphere as observed
 500 by the Viking retarding potential analyzers, *J. Geophys. Res.*, 82, 4351–4363,
 501 doi:10.1029/JS082i028p04351.
 502 Hanson, W. B., and G. P. Mantas (1988), Viking electron temperature measurements:
 503 Evidence for a magnetic field in the Martian ionosphere, *J. Geophys. Res.*, 93, 7538 –
 504 7544.
 505 Hartle, R. E., and J. M. Grebowsky (1995), Planetary loss from light ion escape on Venus,
 506 *Adv. Space Res.*, 15(4), 117 –122, doi:10.1016/0273-1177(94)00073-A.
 507 Huebner, W. F., J. J. Keady, and S. P. Lyon (1992), Solar photo rates for planetary
 508 atmospheres and atmospheric pollutants, *Astrophys. Space Sci.*, 195, 1–294.
 509 Kar, J., K. K. Mahajan, and R. Kohli (1996), On the outflow of O_2^+ ions at Mars, *J. Geophys.*
 510 *Res.*, 101(E5), 12747–12752, doi:10.1029/95JE03526.
 511 Krymskii, A. M., T. K. Breus, N. F. Ness, D. P. Hinson, and D. I. Bojkov (2003), Effect of
 512 crustal magnetic fields on the near terminator ionosphere at Mars: Comparison of in situ
 513 magnetic field measurements with the data of radio science experiments on board Mars
 514 Global Surveyor, *J. Geophys. Res.*, 108(A12), 1431, doi:10.1029/2002JA009662.

515 Lillis, R. J., M. O. Fillingim, and D. A. Brain (2011), Three-dimensional structure of the
 516 Martian nightside ionosphere: Predicted rates of impact ionization from Mars Global
 517 Surveyor magnetometer and electron reflectometer measurements of precipitating
 518 electrons, *J. Geophys. Res.*, 116, A12317, doi:10.1029/2011JA016982.
 519 Lillis, R. J., et al. (2015), Characterizing atmospheric escape from Mars today and through
 520 time, with MAVEN, *Space Sci. Rev.*, doi:10.1007/s11214-015-0165-8.
 521 Lundin, R., et al. (1989), First measurements of the ionospheric plasma escape from Mars,
 522 *Nature*, 341, 609 – 612.
 523 Lundin, R., A. Zakharov, R. Pellinen, S. W. Barabasz, H. Borg, E. M. Dubinin, B. Hultqvist,
 524 H. Koskinen, I. Liede, and N. Pissarenko (1990), Aspera/Phobos measurements of the ion
 525 outflow from the martian ionosphere, *Geophys. Res. Lett.*, 17, 873– 876.
 526 Lundin, R., et al. (2004), Solar wind-induced atmospheric erosion at Mars: First results from
 527 ASPERA-3 on Mars Express, *Science*, 305, 1933–1936.
 528 Lundin, R., H. Lammer, and I. Ribas (2007), Planetary magnetic fields and solar forcing:
 529 Implications for atmospheric evolution, *Space Sci. Rev.*, 129(1–3), 245–278,
 530 doi:10.1007/s11214-007-9176-4.
 531 Ma, Y., A. F. Nagy, K. C. Hansen, and D. L. DeZeeuw (2002), Three-dimensional
 532 multispecies MHD studies of the solar wind interaction with Mars in the presence of
 533 crustal fields, *J. Geophys. Res.*, 107(A10), 1282, doi:10.1029/2002JA009293.
 534 Ma, Y. J., X. Fang, A. F. Nagy, C. T. Russell, and G. Toth (2014), Martian ionospheric
 535 responses to dynamic pressure enhancements in the solar wind, *J. Geophys. Res. Space*
 536 390 Physics, 119, 1272–1286, doi:10.1002/2013JA019402
 537 Matta, M. M. (2013), Modeling the Martian Ionosphere, PhD, Boston Univ., Boston, Mass.

538Matta, M., M. Galand, L. Moore, M. Mendillo, and P. Withers (2014), Numerical simulations
 539 of ion and electron temperatures in the ionosphere of Mars: Multiple ions and diurnal
 540 variations, *Icarus*, 227, 78–88, doi:10.1016/j.icarus.2013.09.006.

541Matta, M., M. Mendillo, P. Withers, and D. Morgan (2015), Interpreting Mars ionospheric
 542 anomalies over crustal magnetic field regions using a 2-D ionospheric model, *J. Geophys.*
 543 *Res. Space Physics*, 120, 766–777, doi:10.1002/2014JA020721.

544Mahaffy, P. R., M. Benna, M. Elrod, R. V. Yelle, S. W. Bougher, S. W. Stone, and B. M.
 545 Jakosky (2015a), Structure and composition of the neutral upper atmosphere of Mars
 546 from the MAVEN NGIMS investigation, *Geophys. Res. Lett.*, 42, 8951–8957,
 547 doi:10.1002/2015GL065329.

548Mahaffy, P. R., et al. (2015b), The neutral gas and ion mass spectrometer on the Mars
 549 Atmosphere and Volatile Evolution mission, *Space Sci. Rev.*, doi:10.1007/s11214-014-
 550 0091-1.

551Nagy A. F., D. Winterhalter, K. Sauer, T. E. Cravens, S. Brecht, C. Mazelle, D. Crider, E.
 552 Kallio, A. Zakharov, E. Dubinin, M. Verigin, G. Kotova, W. I. Axford, C. Bertucci, and
 553 J. G. Trotignon (2004), The plasma environment of Mars, *Space Sci. Rev.*, 111, 33-114,
 554 doi:/10.1023/B:SPAC.0000032718.47512.92.

555Nagy, A. F., and T. E. Cravens (1988), Hot oxygen atoms in the upper atmospheres of Venus
 556 and Mars, *Geophys. Res. Lett.*, 15, 433-435.

557Pepin, R.O., Evolution of the Martian Atmosphere, 1994. *Icarus*, 111, 289-304.

558Rohrbaugh, R. P., J. S. Nisbet, E. Bleuler, and J. R. Herman (1979), The effect of
 559 energetically produced O_2^+ on the ion temperatures of the Martian thermosphere, *J.*
 560 *Geophys. Res.*, 84, 3327 – 3338.

561 Schunk, R. W. and Nagy, A. F., (2009) *Ionospheres*, 2nd Ed. Cambridge University Press,
 562 Cambridge.
 563 Sackmann, I. J., and A. I. Boothroyd (2003), Our Sun. V. A bright young Sun consistent with
 564 helioseismology and warm temperatures on ancient Earth and Mars, *Ap. J.*, 583, 1024–
 565 1039.
 566 Witasse O., T. Cravens, M. Mendillo, J. Moses, A. Kliore, A. Nagy, and T. Breus (2008),
 567 Solar System Ionospheres, *Space Sci. Rev.*, 139, 235-265, doi:/10.1007/s11214-008-
 568 9395-3.
 569 Withers, P. (2009), A review of observed variability in the dayside ionosphere of Mars, *Adv.*
 570 *Space Res.*, 44, 277–307, doi:10.1016/j.asr.2009.04.027.
 571 Withers, P., K. Fallows, and M. Matta (2014), Predictions of electron temperatures in the
 572 Mars ionosphere and their effects on electron densities, *Geophys. Res. Lett.*, 41, 2681–
 573 2686, doi:10.1002/2014GL059683.
 574
 575
 576
 577
 578
 579
 580
 581
 582
 583

Table 1: Photochemical Reactions used in 1D CAPIT

Reaction (Ionization)	Rate (s⁻¹) Moderate Sun	Reference
$\text{N}_2 + \gamma \rightarrow \text{N}_2^+ + \text{e}^-$	2.80×10^{-7}	<i>Huebner et al., 1992</i>
$\text{CO}_2 + \gamma \rightarrow \text{CO}_2^+ + \text{e}^-$	5.30×10^{-7}	<i>Huebner et al., 1992</i>
$\text{O} + \gamma \rightarrow \text{O}^+ + \text{e}^-$	2.00×10^{-7}	<i>Huebner et al., 1992</i>
$\text{O}_2 + \gamma \rightarrow \text{O}_2^+ + \text{e}^-$	4.40×10^{-7}	<i>Huebner et al., 1992</i>
$\text{NO} + \gamma \rightarrow \text{NO}^+ + \text{e}^-$	10.1×10^{-7}	<i>Huebner et al., 1992</i>
$\text{CO} + \gamma \rightarrow \text{CO}^+ + \text{e}^-$	3.44×10^{-7}	<i>Huebner et al., 1992</i>
Reaction (Electron)	Rate (cm³/s)	Reference
$\text{N}_2^+ + \text{e}^- \rightarrow \text{N} + \text{N}$	$2.2 \times 10^{-7} (300/T_e)^{0.39}$	<i>Matta, 2013</i>
$\text{CO}_2^+ + \text{e}^- \rightarrow \text{CO} + \text{O}$	$4.2 \times 10^{-7} (300/T_e)^{0.75}$	<i>Matta, 2013</i>
$\text{O}^+ + \text{e}^- \rightarrow \text{O}$ (not included)	$3.26 \times 10^{-12} (300/T_e)^{0.7}$	<i>Matta, 2013</i>
$\text{O}_2^+ + \text{e}^- \rightarrow 2\text{O}$ (see note)	$2.4 \times 10^{-7} (300/T_e)^{0.7}$	<i>Matta, 2013</i>
$\text{NO}^+ + \text{e}^- \rightarrow \text{NO}$	$4.0 \times 10^{-7} (300/T_e)^{0.5}$	<i>Schunk and Nagy, 2009</i>
$\text{CO}^+ + \text{e}^- \rightarrow \text{CO}$	$2.75 \times 10^{-7} (300/T_e)^{0.55}$	<i>Schunk and Nagy, 2009</i>
Reaction	Rate at 300 °K (cm³/s)	Reference
$\text{N}_2^+ + \text{O} \rightarrow \text{O}^+ + \text{N}_2$	9.8×10^{-12}	<i>Matta, 2013</i>
$\text{N}_2^+ + \text{O} \rightarrow \text{NO}^+ + \text{N}$	1.3×10^{-10}	<i>Matta, 2013</i>
$\text{N}_2^+ + \text{NO} \rightarrow \text{NO}^+ + \text{N}_2$	4.1×10^{-10}	<i>Schunk and Nagy, 2009</i>
$\text{N}_2^+ + \text{O}_2 \rightarrow \text{O}_2^+ + \text{N}_2$	5.0×10^{-11}	<i>Schunk and Nagy, 2009</i>
$\text{N}_2^+ + \text{CO}_2 \rightarrow \text{O}_2^+ + \text{N}_2$	8.0×10^{-10}	<i>Matta, 2013</i>
$\text{CO}^+ + \text{O} \rightarrow \text{O}^+ + \text{CO}$	1.4×10^{-10}	<i>Schunk and Nagy, 2009</i>
$\text{CO}^+ + \text{CO}_2 \rightarrow \text{CO}_2^+ + \text{CO}$	1.1×10^{-9}	<i>Schunk and Nagy, 2009</i>
$\text{CO}_2^+ + \text{O} \rightarrow \text{O}^+ + \text{CO}_2$	9.6×10^{-11}	<i>Matta, 2013</i>
$\text{CO}_2^+ + \text{O} \rightarrow \text{O}_2^+ + \text{CO}$	1.6×10^{-10}	<i>Matta, 2013</i>
$\text{CO}_2^+ + \text{NO} \rightarrow \text{NO}^+ + \text{CO}_2$	1.23×10^{-10}	<i>Schunk and Nagy, 2009</i>
$\text{CO}_2^+ + \text{O}_2 \rightarrow \text{O}_2^+ + \text{CO}_2$	5.0×10^{-11}	<i>Barth, 1985</i>
$\text{O}^+ + \text{N}_2 \rightarrow \text{NO}^+ + \text{N}$	1.2×10^{-12}	<i>Matta, 2013</i>
$\text{O}^+ + \text{O}_2 \rightarrow \text{O}_2^+ + \text{O}$	2.1×10^{-11}	<i>Schunk and Nagy, 2009</i>
$\text{O}^+ + \text{NO} \rightarrow \text{NO}^+ + \text{O}$	8.0×10^{-13}	<i>Schunk and Nagy, 2009</i>
$\text{O}^+ + \text{CO}_2 \rightarrow \text{O}_2^+ + \text{CO}$	1.1×10^{-9}	<i>Matta, 2013</i>
$\text{O}_2^+ + \text{NO} \rightarrow \text{NO}^+ + \text{O}_2$	4.6×10^{-10}	<i>Schunk and Nagy, 2009</i>

587 **Figures**

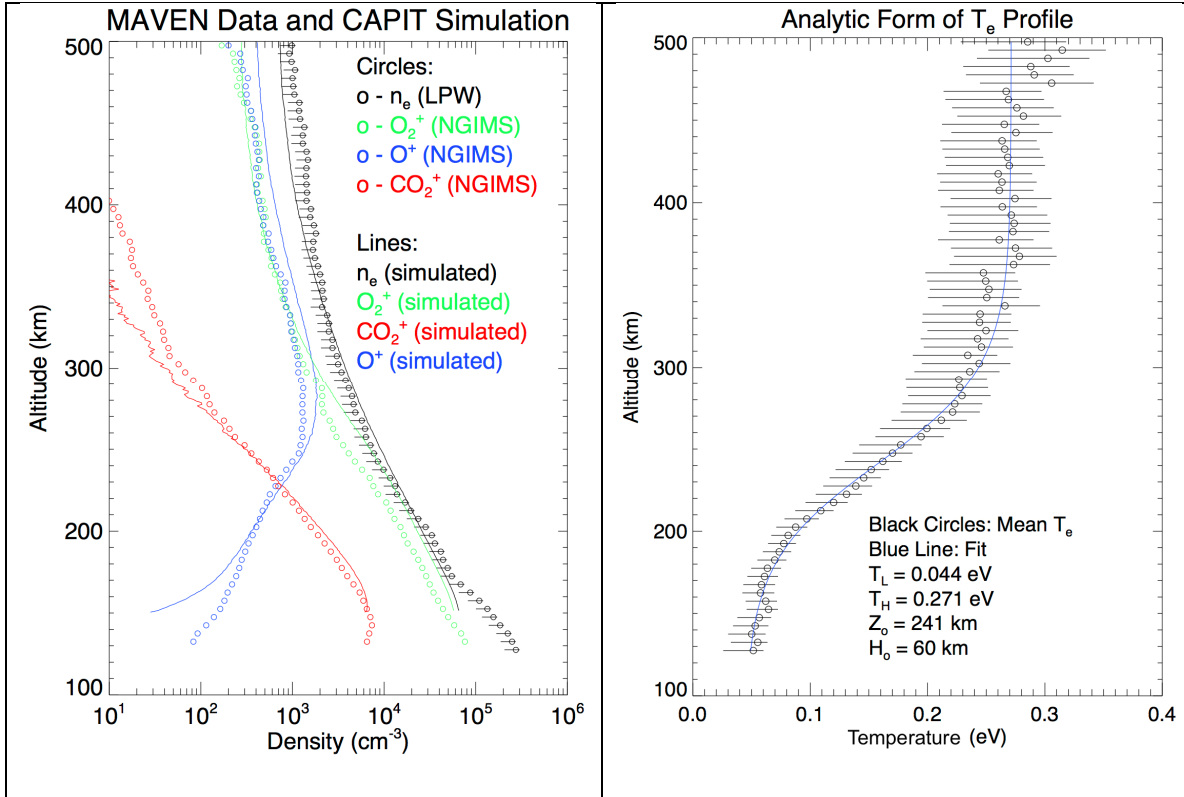


Figure 1. (Left) The average altitude profiles of O_2^+ , O^+ , CO_2^+ , and electron densities during a deep dip campaign from between April 17, 2015 to April 22, 2015. The green circles represent the average altitude profile of O_2^+ , the blue circles represent O^+ , and the red circles represent CO_2^+ . O_2^+ , O^+ , and CO_2^+ densities are measured by NGIMS. The black circles are the electron density measured by the LWP instrument; the horizontal lines reflect the uncertainty. The solid lines with corresponding colors are the results from the 1D CAPIT simulation using the measured electron temperature as input. A Poynting flux of $\sim 3 \times 10^{-8} \text{ W/m}^2$ produces the best agreement between simulation and observations. (Right) The altitude profile of T_e used in the CAPIT simulation is derived from the measured electron temperature profile [from *Ergun et al.*, 2015]. The variability is $\sim 0.1 \text{ eV}$ to $\sim 0.5 \text{ eV}$ from orbit to orbit (see Figure 4, *Ergun et al.*, 2015).

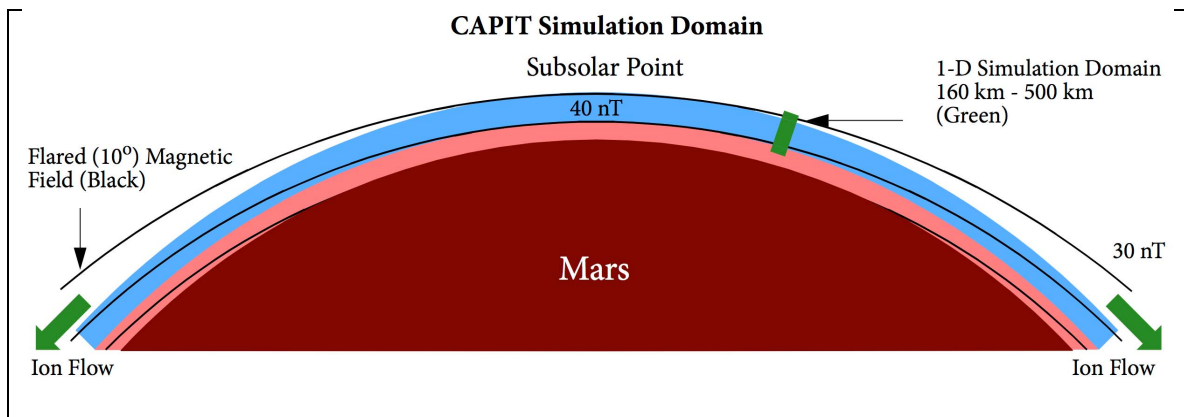


Figure 2. The simulation domain of the CAPIT model. The 2D CAPIT code includes the domain shaded in blue. The 1D CAPIT model, shaded in green, allows for motion along the draped magnetic field lines but no variation in the horizontal direction. The flare angle of the magnetic field is constant at 10° . The drawing is not to scale.

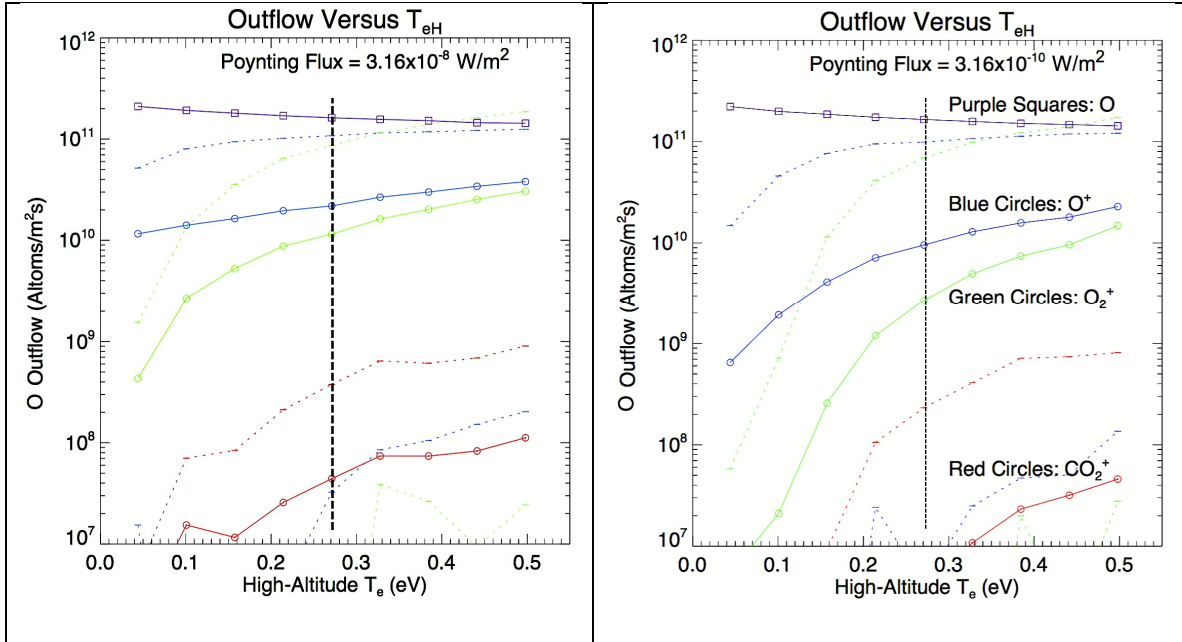


Figure 3. (Left) Estimated outflow versus high-altitude electron temperature from the 1D CAPIT code with weak pointing flux of $3.16 \times 10^{-10} \text{ W/m}^2$. The purple squares and line represent the estimated outflow of O from dissociative recombination of O_2^+ . The blue circles and line are the estimated outflow of O^+ . Green represents O_2^+ and red represents CO_2^+ . The dashed lines indicate the maximum outflow (F_{max}) and the minimum outflow (F_{min}). One can see a strong increase in O_2^+ outflow with increasing electron temperatures. Vertical dashed lines show measured average T_{eH} . (Right) Outflow versus T_{eH} with nominal values of low-frequency Poynting Flux ($3.16 \times 10^{-8} \text{ W/m}^2$). Outflow is larger at low electron temperatures due to the ion heating.

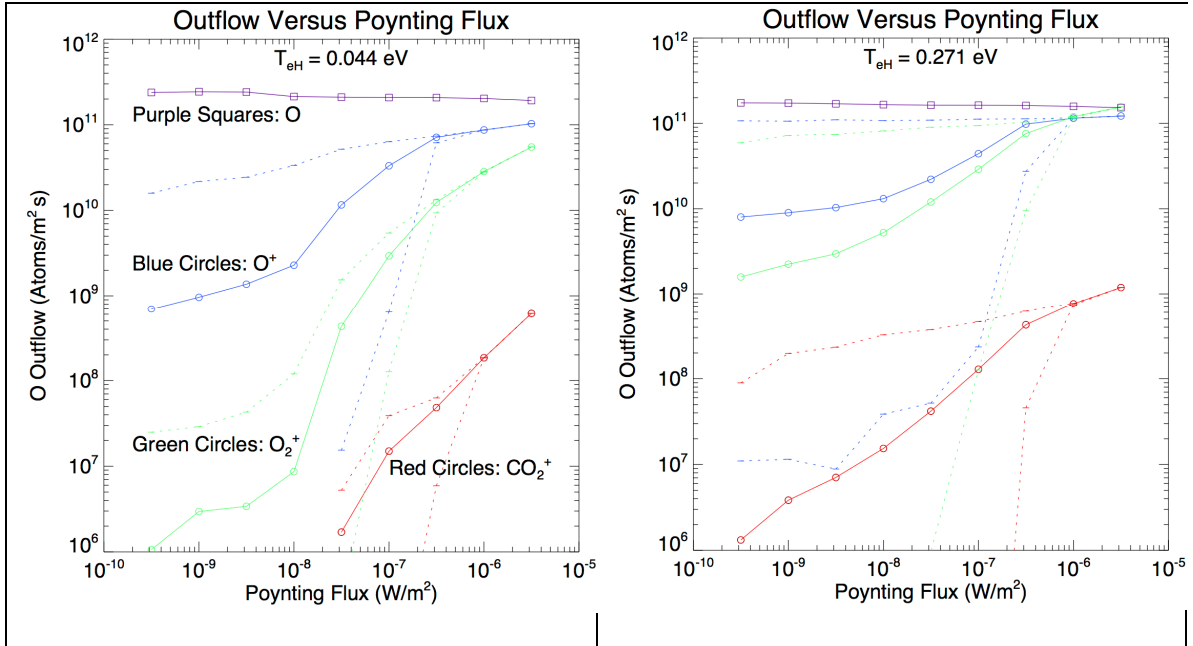


Figure 4. (Left) Outflow versus low-frequency Poynting flux (ion heating) from the 1D CAPIT code with low T_{eH} (0.044 eV). The purple squares and line represent the estimated outflow of O from dissociative recombination of O_2^+ . The blue circles and line are the estimated outflow of O^+ . Green represents O_2^+ and red represents CO_2^+ . The dashed lines indicate the maximum outflow (F_{max}) and the minimum outflow (F_{min}). One can see a strong increase in O^+ and O_2^+ outflow with increasing low-frequency Poynting flux. (Right) Outflow versus low-frequency Poynting flux with nominal values of T_{eH} (0.271 eV). Outflow is larger at low electron temperatures due to the ambipolar electric field.

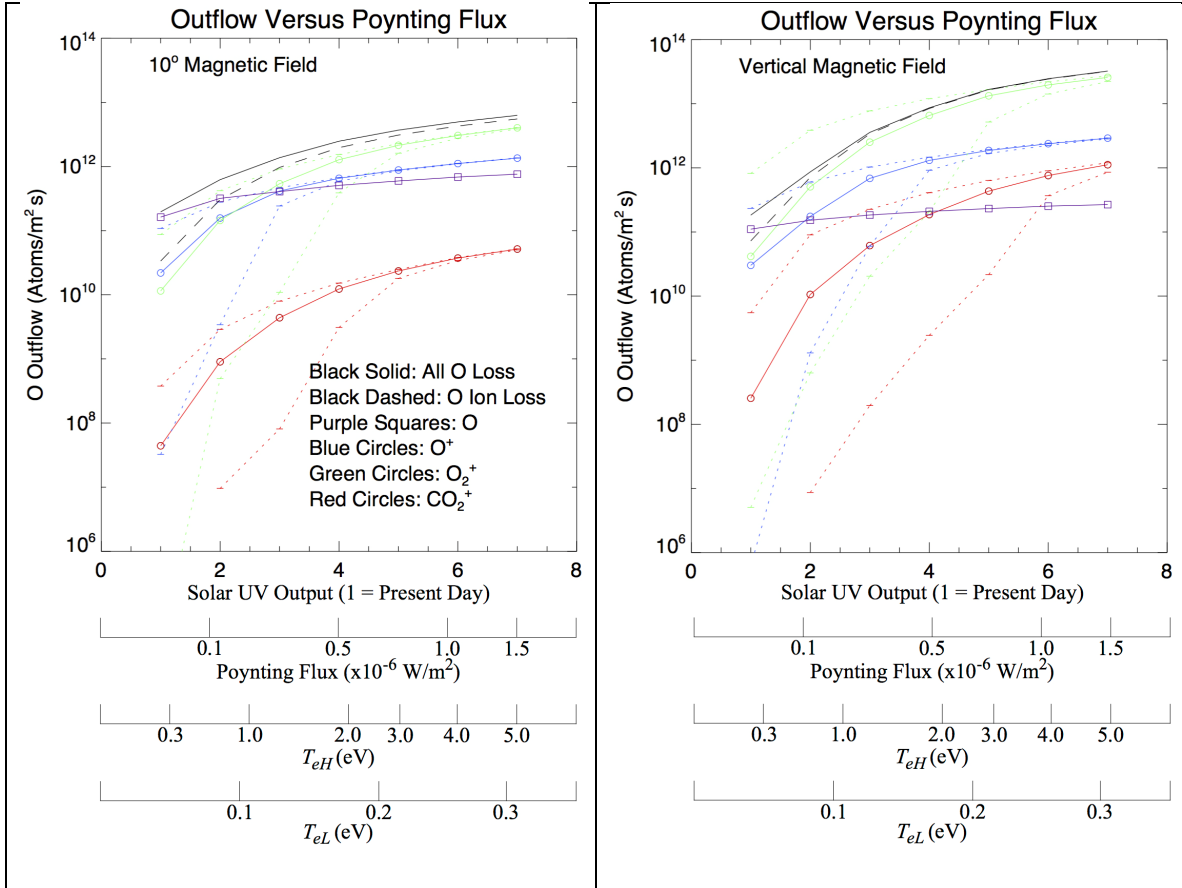
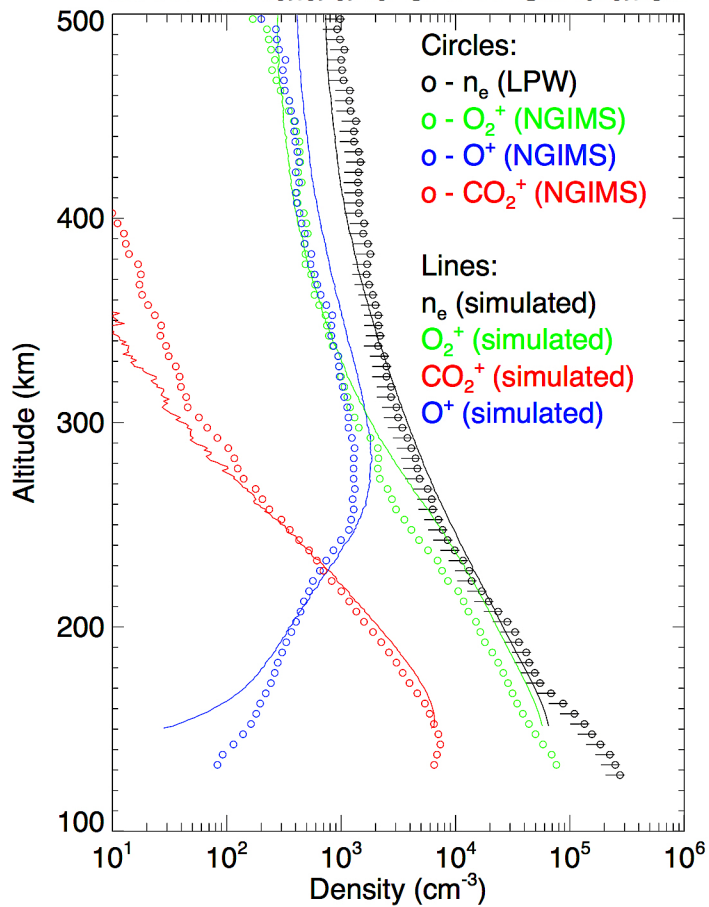
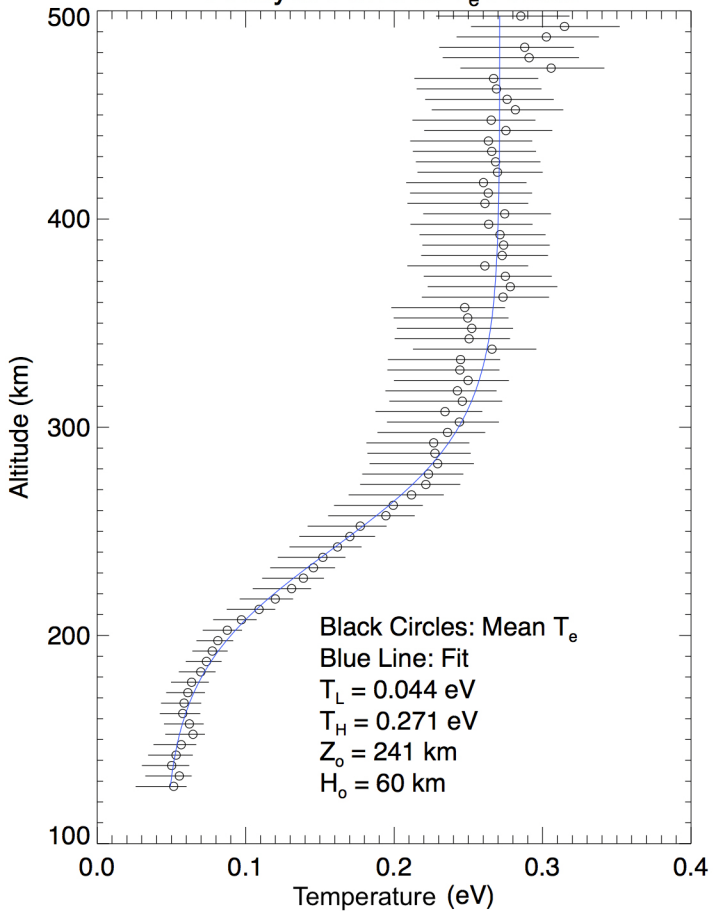


Figure 5. Outflow versus solar output. The color scheme is the same as in Figures 3 and 4. The Poynting flux increases as the square of the solar UV output and T_{eH} is increased as the solar output to the 3/2 power. The left panel has a draped magnetic field at 10°. The right panel has a vertical magnetic field. With the 10° magnetic field, ion outflow exceeds that of dissociative recombination by nearly an order of magnitude under strong solar UV fluxes and strong electron and ion heating. With a vertical magnetic field, ion outflow can reach values resulting in substantial atmospheric loss.

MAVEN Data and CAPIT Simulation



Analytic Form of T_e Profile



CAPIT Simulation Domain

Subsolar Point

1-D Simulation Domain
160 km - 500 km
(Green)

40 nT

Flared (10°) Magnetic
Field (Black)

30 nT

Mars

Ion Flow

Ion Flow

